The Astrophysical Journal, 868:147 (13pp), 2018 December 1 https://doi.org/10.3847/1538-4357/aaeb20

Atmospheric Circulation and Thermal Phase-curve Offset of Tidally and Nontidally Locked Terrestrial Exoplanets

James Penn and Geoffrey K. Vallis
University of Exeter, UK; jp492@exeter.ac.uk, g.vallis@exeter.ac.uk
Received 2018 July 16; revised 2018 October 5; accepted 2018 October 22; published 2018 December 4

Abstract

Using an idealized general circulation model, we investigate the atmospheric circulation of Earth-like terrestrial planets in a variety of orbital configurations. We relax the common assumption of the planet being tidally locked and look at the role atmospheric dynamics can have in the observed thermal phase curve when the substellar point is nonstationary. In slowly rotating planets, a moving forcing can induce strong jets in the upper troposphere, both prograde and retrograde, sensitive to the speed and direction of the diurnal forcing. We find that, consistent with previous shallow-water model experiments, the thermal phase-curve offset is sensitive to the velocity of the substellar point moving across the surface of the planet. For a planet with a known orbital period, the results show that the observed hot spot on the planet could be either east or west of the substellar point, depending on whether the planet is tidally locked or not.

Key words: planets and satellites: atmospheres

1. Introduction

As computing power and model parameterizations improve, the field of dynamical modeling of exoplanetary atmospheres is becoming increasingly sophisticated. For many of the more well-characterized planets, hot Jupiters in particular, we have comprehensive studies of atmospheric circulation (Kataria et al. 2013; Showman et al. 2015; Komacek & Showman 2016, for example) varying from relatively simple Newtonian relaxation (Menou & Rauscher 2009) to highly parameterized studies including full radiation codes and disequilibrium chemistry (Cooper & Showman 2006).

There has also been an effort to design a thermal relaxation benchmark for intercomparison of models of tidally locked exoplanets (Heng et al. 2011) drawing on the knowledge gained from this idealization for Earth modeling, first proposed as a general circulation model (GCM) dynamical core intercomparison benchmark by Held & Suarez (1994).

It is likely that many of the exoplanets discovered to date are tidally locked; due to their close-in orbit of the host star, the effects of tidal friction lead to a slowing of the planetary rotation rate until it is resonant with the orbital rate. However, this is not true of all planets, as is evident from a quick survey of our own solar system. Hot Jupiters, very large gas planets that are very close to their host star, are subject to strong tidal dissipation forces and so are largely expected to be in synchronous orbit; but it is possible that atmospheric winds and internally asynchronous torque forces can force a planet to remain out of a fully tidally locked state (Showman & Guillot 2002). There is evidence that this can be the case for rocky planets, too; Venus's rotation rate is close to synchronous with its orbit, yet thermal tides generated in its thick atmosphere are sufficient to induce a slow retrograde diurnal cycle (Ingersoll & Dobrovolskis 1978). And recent numerical models have shown that even close-in rocky exoplanets could be in asynchronous rotation due to the torque induced from an atmospheric thermal tide (Leconte et al. 2015).

The observational detection bias toward large, close-in planets has necessarily driven much of the modeling research effort into tidally locked exoplanets. With the assumption of tidal locking, the more observationally difficult parameter of planetary rotation rate can be inferred from the easily observable orbital rate of a planet; when a planet is tidally locked, orbital and rotation rates are equal.

Merlis & Schneider (2010) provided a benchmark study for comparing slow- and fast-rotating Earths in a more complex, moist model that includes the effects of an advected water vapor through both latent heat release and radiative feedback. In this framework, it is shown that the outgoing longwave radiation (OLR) distribution on a tidally locked Earth is strongly dependent on rotation rate. The quickly rotating case exhibits a Matsuno–Gill pattern in OLR (Matsuno 1966; Gill 1980), with the peak temperatures occurring in trapped Rossby waves west of the substellar point.

The circulation of tidally locked Earth-like planets has also been considered with detailed land, aquaplanet, and cloud resolving parameterizations (Edson et al. 2011). There it was shown that as the rotation rate is reduced from the mean Earth reference, there occurs a sharp regime change from midlatitude jets to equatorial superrotation at a critical rotation rate; the exact value is dependent on the surface parameterization, but it was shown to indeed be a sharp transition.

Equatorial superrotation is an important dynamical feature that is seen in a wide range of exoplanet models, with slow rotation and large-scale asymmetric forcing expected of tidally locked hot Jupiters and terrestrial exoplanets orbiting low-mass stars (Kopparapu et al. 2016). It is also observable in the solar system; Venus, a slowly rotating terrestrial planet, has a strong superrotating jet at the equator.

Nearly all dynamical models of tidally locked hot Jupiters exhibit a broad superrotating jet transporting heat from the substellar to antistellar point along the equator. Showman & Polvani (2011) used a single shallow-water model to show that the equatorial superrotation can be reproduced in the steady-state Matsuno–Gill framework when modified to include a mass source term from interaction with an underlying quiescent atmospheric layer. The superrotating jet is a consequence of large-scale tropical wave forcing.

The equatorial superrotation provides a strong eastward advective force (in this paper, without loss of generality, we will only consider planets rotating in the same directional sense as Earth, and for the sake of clarity, we use Earth-like nomenclature, so that "eastward" relates to motion prograde with respect to rotation, increasing in longitude). There is a large temperature forcing gradient between the day- and nightsides; the atmospheric heat content generated at the substellar point is efficiently transported by this jet to the cold nightside. The eastward offset has been a common feature of exoplanets for which sufficient observational evidence has been gathered to generate a thermal phase curve. For example, the hot Jupiter HD 189733b has an observed eastward offset of 16° E (Knutson et al. 2007), and, more recently, the close-in super-Earth 55 Cancri e was shown to have an eastward thermal phase-curve offset of 40°E (Demory et al. 2016). The eastward offset of thermal maxima correlates well with the results of dynamical models of tidally locked hot Jupiters and Earth-like exoplanets. The spatially large-scale forcing imposed by a tidally locked heating profile forces the atmosphere in the wavenumber 1 and 2 modes at the equator, producing an eddy flux convergence that drives and maintains the superrotational state (Kraucunas & Hartmann 2005). This advective heat transport is observed in the infrared phase curve of simulated planets, resulting in an eastward offset of the hottest point from the substellar point.

In a previous study (Penn & Vallis 2017), we used a shallow-water model of the atmosphere to investigate the impact of relaxing the assumption of tidal locking has on the atmospheric circulation of a planet, specifically the effect that may be observed remotely through the offset of the thermal phase curve. We demonstrated that in this model of the first baroclinic mode, the phase-curve offset is sensitive to both the orbital and rotation rates of the planet. When the planet is nontidally locked, the hottest region on the planet—corresponding to the peak in observed thermal phase curve—can be offset either to the east or west of the substellar point. The sign and magnitude of the offset were shown to be dependent on the internal wave speed of the atmosphere.

Penn & Vallis (2017) showed that in the shallow-water model, the offset in the thermal phase curve is proportional to the ratio of the substellar velocity to the internal gravity wave speed of the first baroclinic mode. When the substellar point is moving faster than wave speed, in general, the hottest point lags behind the substellar point; if you were standing on the surface, this would correspond to the hottest time of day occurring in the afternoon. However, when the diurnal cycle is slower, it was shown that the hottest point could in some cases lead ahead of the substellar point, giving a thermal maxima before the stellar zenith.

In this study, we extend the shallow-water theory into a three-dimensional, vertically stratified domain and examine the thermodynamic response to a moving stellar forcing. There have been previous studies modeling nontidally locked planets. Focusing on the habitability of potential Earth-like exoplanets, Salameh et al. (2018) explored the effect of slowing the rotation rate of a complex model of Earth with clouds and sea-ice albedo feedback while keeping the orbital period constant, thus extending the length of a day as it slows. It was shown that cloud-induced cooling is reduced when the planet is in nonsynchronous rotation, due to the advection of cloud to the west of the substellar point, lowering planetary albedo at the brightest point. Hot Jupiter HD 189733b has been modeled in both synchronous and asynchronous rotation (Showman et al. 2009), the extent of asymmetry between orbital and planetary rotation rates causing a significant shift in the position of the phase-curve peak of the thermal emission spectra. In a similar vein to our shallow-water model, Rauscher & Kempton (2014) examined the possibility of inferring the planetary rotation rate from the phase-curve observations of asynchronously rotating hot Jupiters. Again studying HD 189733b and HD 209458b, they found that it was possible to observe both eastward and westward offsets of the planetary hot spot relative to substellar zenith. A comprehensive study of hot Jupiters in nonsynchronous rotation (Showman et al. 2015) demonstrated the relationship between the atmospheric radiative timescale and the diurnal timescale. It was shown that the dynamics undergoes a regime change when the ratio of these timescales goes through unity, transitioning from equatorial superrotation in slowly rotating/highly irradiated planets to off-equatorial midlatitude jets more similar to those observed on Earth in quickly rotating systems where zonal temperature gradients are typically much smaller than the equator–pole difference.

These studies have largely focused on hot Jupiters, typically in a parameter space constrained to explore the possible configurations of specific candidate planets. Here we take an idealized approach to the problem, considering a generalized exoplanet and making a systematic investigation of the parameter space encompassed by differential planetary and orbital rotation rates in an approach similar to other exoplanet studies exploring the parameter space around Earth (Merlis & Schneider 2010; Heng et al. 2011; Kaspi & Showman 2015).

2. Model

2.1. Orbital Mechanics

Given the infinitude of possible orbital configurations, we make a few assumptions to constrain our parameter space to a manageable size. We are interested in the dynamics in response to a diurnal forcing; specifically, around the configuration of tidal locking and in the regime where the timescale of daily forcing is similar to those of wave propagation and thermal relaxation in the atmosphere. We assume a circular orbit with zero rotational obliquity; therefore, the planet has no seasonal cycle but can still have a periodic diurnal cycle. It is beyond the scope of this study to investigate the effect of these parameters, but it is certain that they will affect the climate of an exoplanet and observed characteristics. Selsis et al. (2013) modeled close-in "super-Mercuries" around low-mass stars. Even without the inclusion of a dynamic atmosphere, it is shown that the thermal inertia of the surface of a nontidally locked planet on an eccentric orbit leads to complex heat distribution on the surface and, as a result, large changes in the amplitude and offset of an observed phase curve. We leave this natural extension of the model for future investigation.

For a planet with orbital rate Γ, rotation rate Ω, no obliquity, and no eccentricity, the diurnal period is given by

$$P_{\rm sol} = \frac{2\pi}{\Gamma - \Omega}. \tag{1}$$

The length of a stellar day on a planet is thus $T_{\rm sol} = |P_{\rm sol}|$, and here we are also conscious of the sign of the period. A negative value indicates that, as on Earth, the substellar point will

progress from east to west across the surface of the planet; positive values give a prograde progression, as on Venus.

At time t, the substellar point is located at longitude

$$\lambda_0(t) = 2\pi\frac{t}{P_{\rm sol}} = (\Gamma - \Omega)t. \tag{2}$$

For a tidally locked planet, $\Omega = \Gamma$, and therefore the substellar point remains stationary. For a nontidally locked planet, the substellar velocity at the equator in the zonal direction is given by the differential of orbital and planetary rotation rates. Given a planetary radius a (here held constant at Earth's value, $a = 6371$ km), we can write this as a velocity in a local zonal coordinate x,

$$\frac{dx_0}{dt} = a(\Gamma - \Omega) \equiv s. \tag{3}$$

2.2. Dynamical Model

We model the shallow atmosphere of an Earth-like planet using the dry, hydrostatic primitive equations and parameterize the effect of stellar forcing and radiative transfer with a linear relaxation of the temperature toward a predefined reference equilibrium profile. The equations are, in pressure vertical coordinates,

$$\frac{D\boldsymbol{u}}{Dt} + \boldsymbol{f}\times\boldsymbol{u} = -\nabla_p\Phi - r\boldsymbol{u}, \tag{4}$$

$$\frac{\partial\Phi}{\partial\ln p} = -RT, \tag{5}$$

$$\nabla_p\cdot\boldsymbol{u} + \frac{\partial\omega}{\partial p} = 0, \tag{6}$$

$$\frac{DT}{Dt} = \frac{\kappa T\omega}{p} + \frac{Q}{c_p}, \tag{7}$$

where the prognostic state variables are the horizontal wind vector $\boldsymbol{u} = (u, v)$, temperature T, and vertical velocity expressed in terms of pressure change $\omega \equiv Dp/Dt$. The total time, or Lagrangian, D/Dt operator in pressure coordinates is given by

$$\frac{D}{Dt} = (\boldsymbol{u}\cdot\nabla_p) + \omega\frac{\partial}{\partial p}, \tag{8}$$

where $\nabla_{\rm p}$ is the horizontal gradient operator along isobaric surfaces.

We solve the equations in spherical coordinates (r, λ, ϕ): radius, longitude, and latitude, respectively. Coriolis force in the traditional approximation is given by $\boldsymbol{f} = \hat{\boldsymbol{k}}2\Omega\sin\phi$. This is a so-called "shallow" approximation, as we ignore the effects of Coriolis forces in the vertical; to conserve angular momentum, we must also assume that flow is confined to a shallow shell on the surface of the sphere. The radial coordinate is expressed as $r = a + z$, where a is the radius of the planet; since $a \gg z$, we make the shallow-fluid approximation by replacing $r \to a$, and $\partial r \to \partial z$. The gravitational force, g, assumed to be constant, is absorbed into a height-proxy geopotential $\Phi \equiv gz$. Here R is the ideal gas constant for dry air, and c_p is the specific heat capacity of dry air at constant pressure, $\kappa = R/c_p$. The equations are solved in pressure coordinates rather than absolute height, so we also have a prognostic equation of surface pressure at the lower boundary,

$$\frac{\partial p_s}{\partial t} = -\nabla\cdot\int_0^{p_s}\boldsymbol{u}dp. \tag{9}$$

The equations are forced through a Newtonian heating term

$$\frac{Q}{c_p} = \frac{T - T_{\rm eq}}{\tau_{\rm rad}}, \tag{10}$$

where $T_{\rm eq}$ is the equilibrium heating profile detailed below, and $\tau_{\rm rad}$ is a characteristic timescale of thermal relaxation of the atmosphere. The system is damped by linear Rayleigh friction in the momentum equation, parameterized by coefficient $r = r(p)$, the inverse of which can be considered as the timescale of frictional forcing.

We use the open-source Isca framework (Vallis et al. 2018), a recently released fork of the Princeton GFDL FMS modeling suite. Isca solves the hydrostatic primitive Equations (4)–(7) on a sphere using a pseudospectral dynamical core in pressure coordinates. All results are from a T42 resolution (approximately 3° notional grid). Full source codes for the model and experiments are available online at https://github.com/execlim/isca.

2.3. Newtonian Heating Profile

The heating profile $T_{\rm eq}$ is calculated from a potential temperature profile $\theta_{\rm eq}$, constructed to approximate the convective–radiative equilibrium state of an Earth-like planet with zero obliquity and eccentricity,

$$\theta_{\rm eq} = \begin{cases} T_0 - \Delta_h(1 - \cos\Theta_s) - \Delta_v\cos\Theta_s\log\dfrac{p}{p_{\rm ref}} & \cos\Theta_s > 0, \\ T_{\rm strat} & \cos\Theta_s < 0, \end{cases} \tag{11}$$

$$T_{\rm eq} = \max\left(\theta_{\rm eq}\left(\frac{p}{p_{\rm ref}}\right)^{\kappa}, T_{\rm strat}\right). \tag{12}$$

Figure 1 shows the shape of the forcing in height and across the surface of the planet. This profile assumes an optically thin atmosphere in the shortwave and no clouds, producing maximal heating at the surface under the substellar zenith, similar to heating from a surface below with zero heat capacity. Relaxation temperatures are constrained by two temperature extremes: T_0 is the heating at the zenith surface, and $T_{\rm strat}$ is the background temperature at the stratosphere and dark side of the planet. The equator-to-pole temperature gradient is $\Delta_h = T_0 - T_{\rm strat}$, and the atmospheric column is marginally statically stable, $\Delta_v = 10\,{\rm K}^{-1}$, such that potential temperature increases gradually throughout the troposphere before becoming very stable in the stratosphere. The zenith angle of the star, Θ_s, provides the diurnal component of the profile; for a planet with zero obliquity and eccentricity, this simplifies to a function of latitude, longitude, and, implicitly, time for planets that are not tidally locked:

$$\cos\Theta_s = \cos\phi\cos(\lambda - \lambda_0(t)). \tag{13}$$

As it will become the useful reference frame for analysis of numerical results, we define a longitudinal coordinate relative to the substellar point, $\xi = \lambda - \lambda_0$.

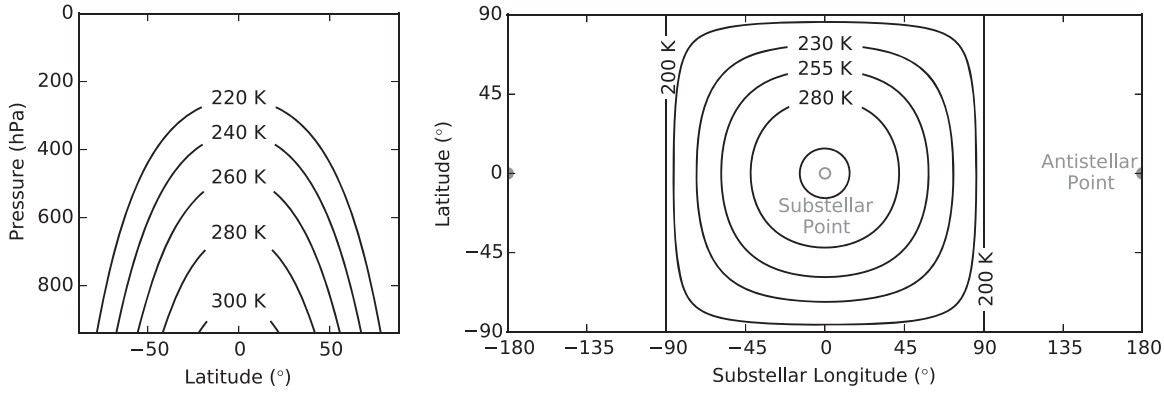

(a) T_{eq} vertical profile (b) T_{eq} horizontal profile

Figure 1. Contour plot of latitude–pressure (a) and latitude–longitude (b) profiles of the relaxation temperature profile $T_{\rm eq}$. The latitude–longitude profile is shown with longitude relative to the substellar point.

As in the formulation of Held & Suarez (1994), we apply a timescale of thermal damping that includes a boundary layer

$$\tau_{\rm rad} = \tau_{\rm atm} + (\tau_{\rm atm} - \tau_{\rm sfc}) \max\left(\frac{p - p_{\rm BL}}{p_s - p_{\rm BL}}, 0\right), \tag{14}$$

where $p_{\rm BL} = 700$ hPa is an empirically derived pressure height for the top of the boundary layer, but we do not scale this damping at the poles, as is done in Earth simulations. Velocity damping is constrained solely to the boundary layer and decreases linearly with height,

$$r = \frac{1}{\tau_{\rm fric}} \max\left(\frac{p - p_{\rm BL}}{p_s - p_{\rm BL}}, 0\right). \tag{15}$$

Constants $\tau_{\rm atm}$, $\tau_{\rm sfc}$, and $\tau_{\rm fric}$ have a nontrivial impact on the dynamics of the atmosphere, but systematic investigation of this dimension of the parameter space is beyond the scope of this study. For radiative relaxation, we choose values $\tau_{\rm sfc} = 5$ days and $\tau_{\rm atm} = 20$ days, such that low-level heating is more tightly coupled to the forcing profile, while at altitude, the timescale of relaxation is longer, more akin to the scale of a purely radiative timescale. Frictional damping, restricted to the planetary boundary layer, is set at $\tau_{\rm fric} = 1$ day.

3. Results and Discussion

The numerical model was run with a range of parameter values of Ω and s, as shown in Table 1. As we are considering the dynamics of a theoretical exoplanet, we do not only restrict the parameter space-specific resonant orbital and rotation configurations; instead, we vary the substellar velocity independently of the rotation rate. In the discussion, we will use Equation (3) to address the question of how this may relate to planets trapped in, e.g., 3:2 orbital resonances, although this may not be a particularly consistent argument given that we keep orbital eccentricity at zero and thus thermal forcing at a constant, implying a circular orbit.

For the sake of clarity, only a representative subset of the parameter space listed in Table 1 is plotted in the following figures, but the complete span of values is considered in the discussion that follows.

The model was integrated forward in time from rest to a statistically steady state. Results presented, unless stated otherwise, are time-averaged over a 100-Earth-day (8.6×10^6 s) window in this steady state and shown in a reference frame relative to the substellar point at 0° longitude.

Table 1
Parameter Values of Rotation Rate and Substellar Velocity

Rotation Rate, Ω	1, 3, 10, 30, 100, 300, 1000	$\times 10^{-7}$ s^{-1}
Substellar Velocity, s	−200, −100, −50, −25, −10, −5, 0, 5, 10, 25, 50, 100, 200	m s^{-1}

3.1. Dynamics

The atmospheric dynamics are dependent on both the rotation rate and substellar velocity. The effects of rotation on tidally locked planets (Noda et al. 2017, for example) and axisymmetrically heated aquaplanets (Kaspi & Showman 2015, for example) have been well studied in recent years; we build upon these results and will not linger too long on discussing the tidally locked cases in isolation, instead focusing on the inclusion of a moving forcing.

We define the planetary Rossby number,

$$\mathrm{Ro} = \frac{U}{\Omega a}, \tag{16}$$

where U is a characteristic zonal velocity as a nondimensional number for characterizing the influence of rotation on the large-scale dynamics. When $\mathrm{Ro} \ll 1$, as is the case on Earth, rotation will constrain atmospheric flow and the dynamical balance of forces, especially away from the equator, will be geostrophic. At large Rossby numbers, rotation plays a much smaller role, pressure gradients largely being balanced by frictional forces. We will show, however, that the addition of a moving heat source in both regimes can alter the large-scale structure of the flow.

Figures 2 and 3 show snapshots of temperature and wind in the mid-troposphere of slowly rotating ($\mathrm{Ro} \sim 10$) and quickly rotating ($\mathrm{Ro} \sim 0.1$) planets in the left and right panels, respectively, after the simulations have been allowed sufficient time to reach a statistical steady state.

Consistent with the first baroclinic mode theory of the previously presented shallow-water model, at slow rotation rates with a slowly moving (or stationary) diurnal cycle, upper-level flow is divergent from the heated hemisphere. To first order, the response to heating is a overturning circulation

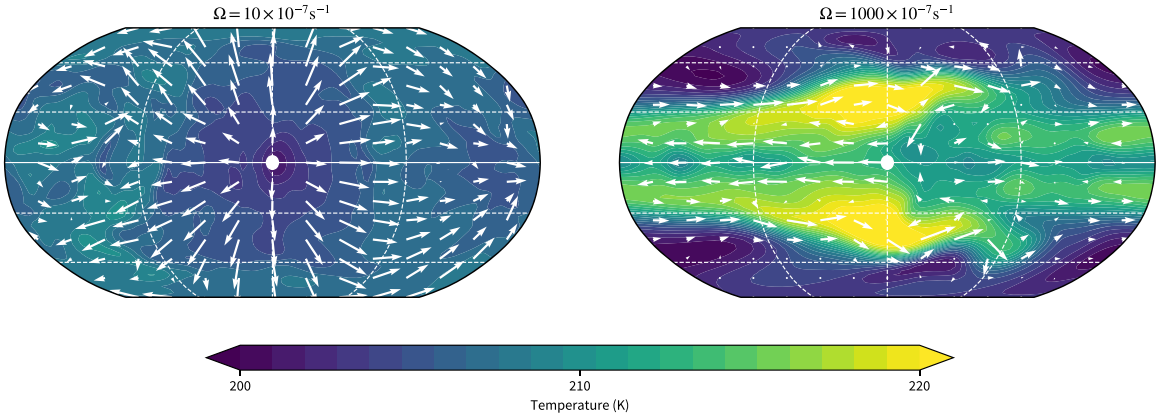

Figure 2. Snapshot of temperature and wind field at the 406 hPa level for tidally locked planets rotating slowly (left) and quickly (right). The substellar point is in the middle of the domain, shown as a white spot. Compare to Figure 3, where the substellar point is moving slowly eastward. The substellar point is in the center, shown by a white spot.

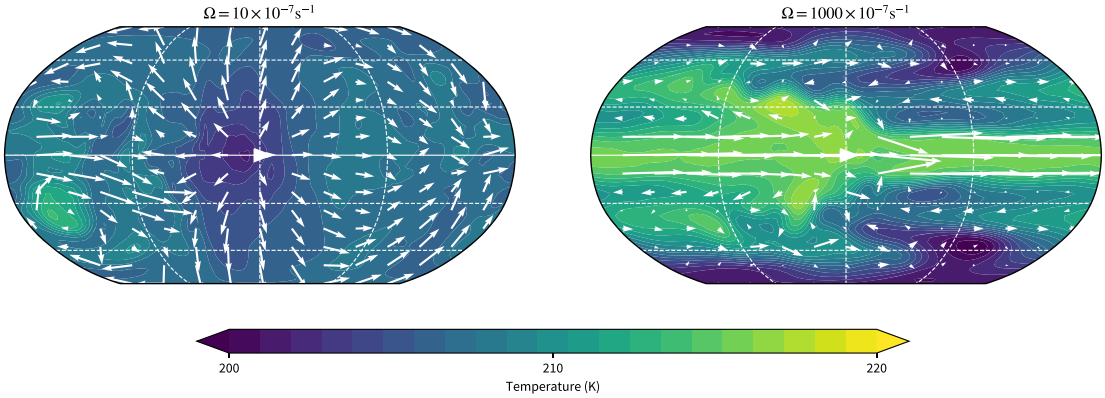

Figure 3. Snapshot of temperature and wind field at the 406 hPa level for nontidally locked planets rotating slowly (left) and quickly (right). The substellar point is moving eastward at 5 m s^{-1}; the substellar point and direction are denoted with a white arrow. Compare to Figure 2, where the substellar point is fixed.

spanning the entire planet, with updraft at the substellar forcing inducing large-scale convergence at the surface and divergence aloft. The weak Coriolis parameter lends little dynamical asymmetry between the meridional and zonal directions, and thus a thermally direct overturning circulation extends from equator to pole, day to night, air rising near the substellar point and eventually falling at the pole or nightside, producing adiabatic heat transport. The largely horizontally uniform temperature on the slowly rotating cases has been well explained by the weak temperature gradient (WTG) approximation (Sobel et al. 2001; Mills & Abbot 2013), and the small Coriolis parameter means that the dominant balance in the dynamical equations is convective between heating and vertical advection of potential temperature.

For quickly rotating planets, circulation is constrained by the Coriolis force, and the response is qualitatively different between a stationary and moving forcing. With a tidally locked stationary configuration, the flow temperature and wind fields display a global Matsuno–Gill pattern of trapped Rossby wave lobes in the midlatitudes west of the center of the forcing, with a small circulation around them and a strong westward flow along the equator west of the substellar point. When even a small prograde velocity is applied to the forcing, the circulation changes dramatically, instead inducing a eastward superrotating jet along the equator, with eddies extending toward the poles.

Figure 4 shows the temporal-mean upper-tropospheric flow for a range of retrograde and prograde substellar velocities at increasing planetary rotation rates. As the substellar velocity increases, increasing-strength zonal jets are induced in the tropics, producing strong superrotation when the progression of substellar points is prograde with respect to rotation. The superrotating jet persists for increasing rotation rate, becoming more equatorially constrained as the planetary Rossby number decreases.

A retrograde moving forcing, as on Earth (although on Earth, the velocity of a substellar point along the equator is ~ -450 m s^{-1}, putting it in a regime well off to the far left of the parameter values studied here), appears to inhibit the formation of a superrotating equatorial jet. Furthermore, a subrotating equatorial flow becomes a robust feature of the atmosphere of slowly rotating planets with a retrograde forcing.

A westward superrotating jet is generated from a substellar point moving westward at 50 m s^{-1} (upper left panel of Figure 4). As the substellar point moves beyond a critical velocity, between ± 50 and 100 m s^{-1}, slow-rotator circulation transitions again, with the upper-level zonal flow weakening and eventually turning off. In these cases, the speed of the substellar point means that the diurnal timescale, $\tau_{\text{diurnal}} = 2\pi a/s$, the time taken for the substellar point to make a complete revolution of the planet, is of the equivalent order as thermal relaxation, τ_{rad}.

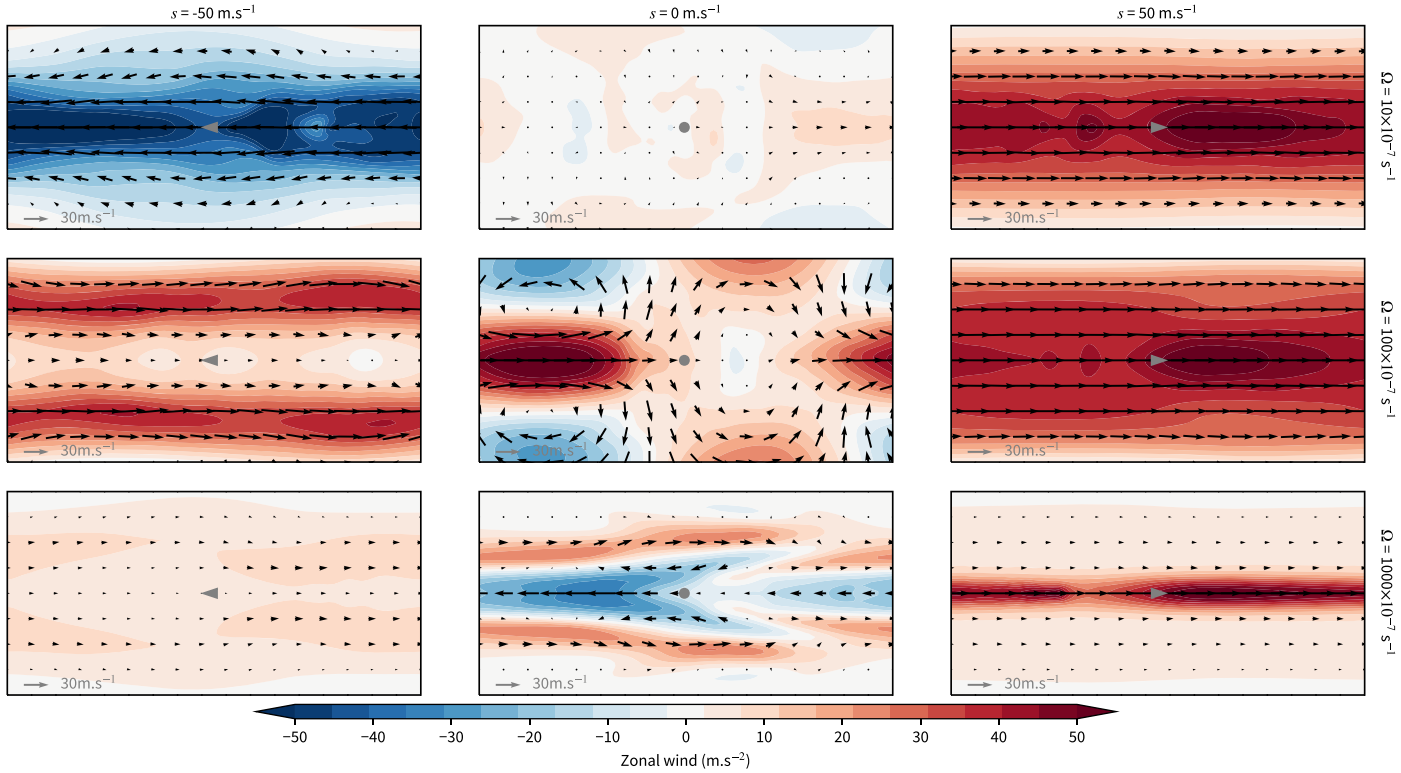

Figure 4. Jet structure in the upper troposphere ($p = 249$ hPa) for increasing rotation rates (rows) and substellar velocities (columns). Vectors indicate the wind, keyed with 30 m s^{-1} in the lower left corner. Colored contours show the zonal component of the mean flow only. The position and direction of motion of the substellar point is indicated with a gray arrowhead.

In the fast-rotating cases (lower half of Figure 4), circulation is dominated by geostrophic forces. The flow becomes latitudinally constrained, but the latitudinal cross-section structure is determined by the direction and speed of the moving forcing. In the fastest-rotation cases, we observe multiple eddy-driven jets being formed, as expected from quasi-geostrophic theory and as seen in the rotation rate parameter studies of Kaspi & Showman (2015). In the intermediate-rotation case, $\Omega = 1 \times 10^{-5}\,\mathrm{s}^{-1}$, the tidally locked and prograde moving substellar point configurations exhibit a single equatorial superrotating jet. When the substellar point is moved sufficiently quickly retrograde to rotation, $s \simeq 50\,\mathrm{m\,s}^{-1}$, the equatorial jet is inhibited, and instead, two midlatitude eastward jets are formed.

The effect of the retrograde moving forcing on the superrotating jet can be more readily observed in the vertical structure of the atmosphere in both the day and night hemispheres (Figure 5). When the Rossby deformation radius is small enough to drive zonal flow but not dominating in the dynamics (the rows labeled $\Omega = 100 \times 10^{-7}\,\mathrm{s}^{-1}$ are rotating approximately $7\times$ slower than Earth and have a Rossby number $\mathrm{Ro} = \mathcal{O}(1)$), a retrograde moving forcing acts in a manner akin to further reducing the Rossby number of the flow, producing a stronger effective rotational regime. This is observed in the inhibition of the superrotating jets produced in the $\mathrm{Ro} = \mathcal{O}(1)$ planet. Figure 6 shows an extended cross-section for varying substellar velocity at a rotation rate $\Omega = 100 \times 10^{-7}\,\mathrm{s}^{-1}$, where, reading from right to left, an increasing retrograde substellar velocity turns off the superrotating equatorial jet and turns on the midlatitudinal jets. At the highest substellar velocities, both prograde and retrograde, $\tau_{\mathrm{diurnal}} \ll \tau_{\mathrm{rad}}$, and the local equilibrium temperature is oscillating as the diurnal cycle passes over at a much quicker rate than the rate of thermal adjustment. The consequence is a "smearing out" of the equilibrium profile. In the limit of infinitely fast substellar progression, the relaxation profile at all longitudes would be the zonal mean of Equation (12), shown in Figure 7. Therefore, on the planets with the fastest-moving substellar points, the forcing felt becomes more zonally symmetric, but also weaker. Hide's theorem (Hide 1969; nicely summarized in Read & Lebonnois 2018) states that given an ideal inviscid fluid, axisymmetric about its rotational vector, for angular momentum to be conserved, it is not possible to maintain a superrotational jet at the equator. To do so requires a longitudinal gradient in the forcing, either via eddies or a large-scale forcing such as the diurnal cycle. This gives further insight into what is happening as the diurnal timescale becomes shorter than the radiative; the effective forcing becomes more axisymmetric, and so superrotation induced by the gradient of the diurnal forcing is diminished.

At the surface, the mean equator-to-pole temperature gradient is less than half that found at the substellar point, reducing the strength of the subtropical zonal jets as expected from the thermal wind relation for the geostrophic component of the zonal wind (Vallis 2017, Section 2.8.4, for example),

$$f\frac{\partial u}{\partial p} = \frac{R}{p}\frac{\partial T}{\partial y}. \tag{17}$$

The magnitude of vertical shear in the zonal winds is proportional to the latitudinal temperature gradient.

In general, the propensity is for eastward flow in both the day and night hemispheres, either in an equatorial superrotating flow or as midlatitude jet structures, where the tidally locked response is in agreement with the previous work of

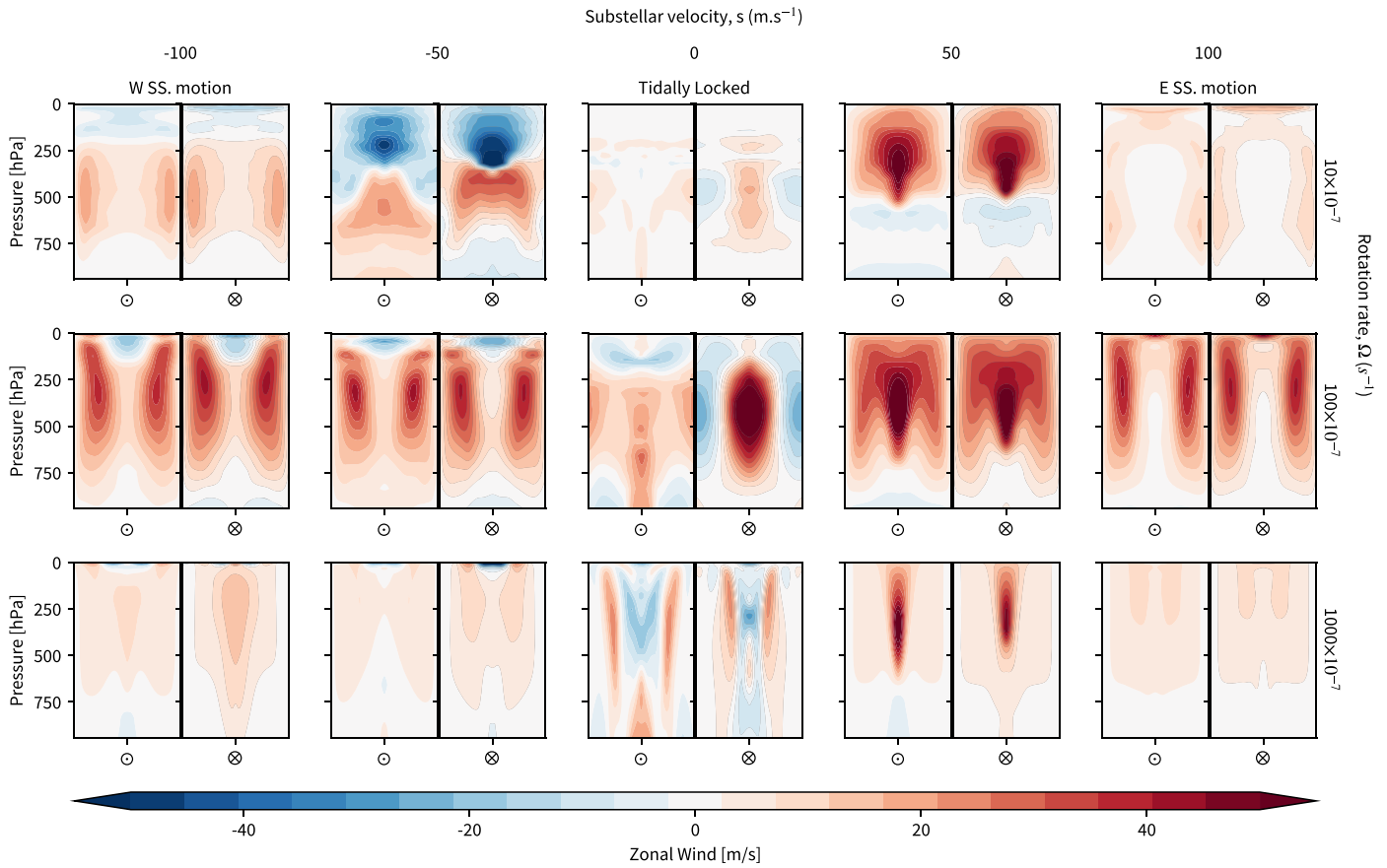

Figure 5. Time-averaged zonal wind latitude–pressure profile at the substellar (⊙) and antistellar (⊗) points. The abscissa in each pane is the latitude from −90° to 90° with the equator denoted by a tick mark.

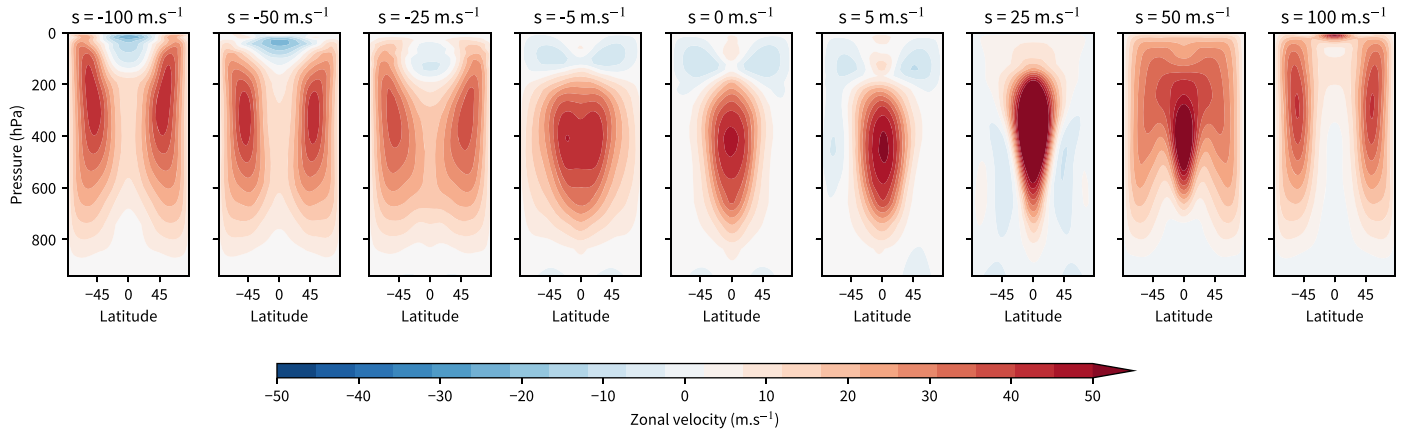

Figure 6. Zonal-mean zonal wind with varying substellar motion, with rotation rate $\Omega = 100 \times 10^{-7}\,\mathrm{s}^{-1}$. From left to right, the panels go from fastest retrograde substellar velocity, through tidally locked, to fastest prograde motion.

Merlis & Schneider (2010), Edson et al. (2011), and Noda et al. (2017). However, at low rotation rates and for intermediate retrograde substellar velocities $100\,\mathrm{m\,s^{-1}} < s < 0\,\mathrm{m\,s^{-1}}$, a westward equatorial jet is generated.

Figure 8 summarizes the above, showing the zonal-mean zonal velocity in the upper troposphere as a function of substellar velocity (abscissa) and rotation rate (lines) for the complete parameter space listed in Table 1. There appears to be a resonant response of the atmosphere at $|s| = 50\,\mathrm{m\,s^{-1}}$ producing the strongest equatorial jets in either direction. And this is the only point in the parameter space for which a significant equatorial subrotating flow is generated: high Rossby number and retrograde substellar progression, $-50 \leqslant s < 0$. As the planetary Rossby number becomes very small ($\Omega \geqslant 100 \times 10^{-7}\,\mathrm{s^{-1}}$), the upper-level zonal flow becomes largely independent of diurnal cycle and substellar velocity.

It can be shown that in the hydrostatic Boussinesq approximation (i.e., constant vertical stratification), the horizontal phase speed of wave propagation in a dry atmosphere is given by

$$c_m = \frac{\omega}{\kappa} = \frac{N}{m}, \tag{18}$$

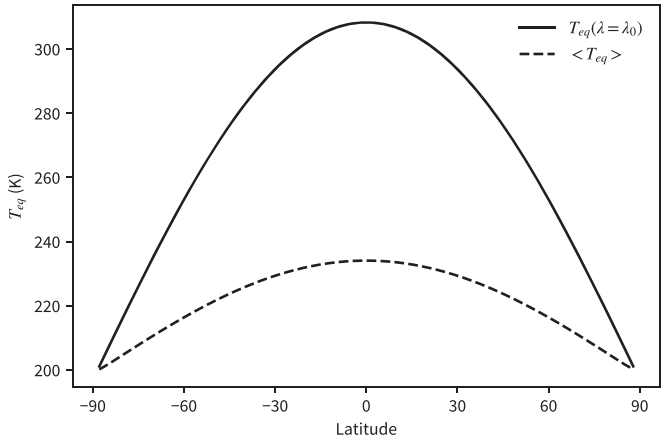

Figure 7. Surface equilibrium temperature gradients at the substellar point (solid) and the zonal mean, $\langle T_{\rm eq}\rangle$ (dashed). The much-reduced $\Delta_{\rm eq-pole}T_{\rm eq}$ in the mean vs. substellar point impacts the dynamics of planets with very quickly moving diurnal cycles.

where $\kappa = k^2 + l^2$ is the horizontal wavevector, and m is the vertical wavenumber (Vallis 2017, Section 7.3). As $m \equiv \pi/H_c$, where H_c is the vertical wavelength, for the $m = 1$ mode, H_c is twice the height of the troposphere, H, and so the fastest wave will be given by

$$c_1 = \frac{NH}{\pi}. \tag{19}$$

The Brunt–Väisälä frequency is defined as

$$N^2 \equiv \frac{g}{\tilde{\theta}}\frac{\partial \tilde{\theta}}{\partial z}, \tag{20}$$

for a mean potential temperature profile $\tilde{\theta}(z)$. Near the surface, N^2 is largely constrained by the short relaxation times and therefore by the equilibrium forcing profile, but aloft, it will be determined dynamically. As a point of reference for this model, the largest ($m = 1$) and fastest-moving mode has been estimated from measurements for the Earth's troposphere, yielding a value $c \simeq 44$ to $-53\,\mathrm{m\,s^{-1}}$ for a deep tropospheric convection in response to moving heat forcing, given a free-tropospheric scale height $H = 14$ km (Kiladis et al. 2009).

We calculate a zonal-mean Brunt–Väisälä frequency and a scale height of the first baroclinic mode, $m = 1$, in the equatorial free troposphere and find that it varies with the substellar velocity (Figure 9), giving local gravity wave speeds between 40 and $60\,\mathrm{m\,s^{-1}}$ in the free troposphere, similar to those of Earth conditions, as we would expect from the essentially Earth-like parameters of the Newtonian cooling model. This suggests that the largest response in the jet structure in the model at substellar velocities moving in either direction at $s \simeq \pm 50\,\mathrm{m\,s^{-1}}$ may be a resonant interaction with the primary gravity wave mode.

Lindzen (1981) demonstrated a theory of internal gravity waves interacting with the mean zonal wind; internal gravity waves moving with a horizontal phase speed c propagate vertically until they reach a critical level, where $\bar{u} \simeq c$ and the waves break, depositing momentum. Lindzen considered the interaction of gravity waves forced by the Earth's diurnal tide, which has a phase speed of $\sim 450\,\mathrm{m\,s^{-1}}$, much greater than the winds observed in the troposphere. However, in our model of nontidally locked exoplanets, we are in a range where $|s| \simeq |\bar{u}|$; thus, a constructive or destructive deposition of zonal momentum can occur in the troposphere, with a peak response at the maximum internal gravity wave speed of the stratified atmosphere given by Equation (19). As frictional forces weaken with height and, in general, $\partial\bar{u}/\partial z > 0$, we would expect to see the height of maximum momentum deposition, and this is observed in Figure 6—the altitude of peak zonal velocity increases with substellar velocity. Why an overturning circulation is induced aloft (see the large vertical shear above the equator in the $s = \pm 50\,\mathrm{m\,s^{-1}}$, $\Omega = 10 \times 10^{-7}\,\mathrm{s^{-1}}$ panels in Figure 5) requires further study.

It is clear that the horizontal circulation has a dependence on diurnal cycle at low rotation rates; if we were observing these planets from afar, the advective heat transport associated with the flow might be detected as either an eastward or westward offset in the thermal phase curve. In general, the upper-tropospheric mean zonal flow is additively modulated by the moving forcing, especially in high Rossby number regimes where the motion-induced flow is significantly larger than the relatively weak overturning flow of the tidally locked case (Figure 10).

Figure 11 is a schematic overview of the dynamical regimes observed and presented in Figures 4, 5 and 8. The region in which equatorial superrotation occurs is limited to a subset of rotational velocities (clearest in the central column of Figure 5); very slowly rotating planets have a direct circulation in both directions around the planet, akin to two large Hadley-Walker cell circulations extending from substellar to antistellar points and pole to pole.

As discussed above, a retrograde moving forcing has a similar effect on dynamics to increasing the rotation rate, shown schematically in the center of Figure 11; this means that the transition from thermally direct coupling of day and night hemispheres to an equatorial jet moving in the same direction as the forcing occurs at a lower rotation rate when the substellar point is moving retrograde ($s < 0$) than when it moves prograde.

Equatorial superrotation is prevalent in nearly all studies presented here, especially those with slower rotation and diurnal speeds. However, as for the transition away from a thermally direct circulation, the point at which a strongest equatorial superrotating jet is maintained is when the substellar point is progressing prograde (right panels of Figure 6). The distinction in the top section of Figure 11 between mid-latitudinal jets and equatorial jets is not exclusive; both can coexist, especially as the Rossby number becomes sufficiently small that multiple baroclinic jets can be sustained (Kaspi & Showman 2015 provided a good discussion of the emergence of multiple jets on quickly spinning Earth-like planets). Instead, it is intended to demonstrate which may be dominant.

The transition from a forced jet to a superrotating jet for a prograde moving substellar point is somewhat continuous (depicted with a dashed line in Figure 11), but the effect is also additive, the superrotation being sharper and more equatorially constrained in the presence of a prograde moving diurnal cycle.

The diversity of climate regimes at a given rotation rate can largely be understood as a result of the scale of timescales of radiative cooling, advection, and the diurnal cycle. In general, if $\tau_{\rm rad} \ll \tau_{\rm adv}, \tau_{\rm diurnal}$, the radiative forcing dominates, and the

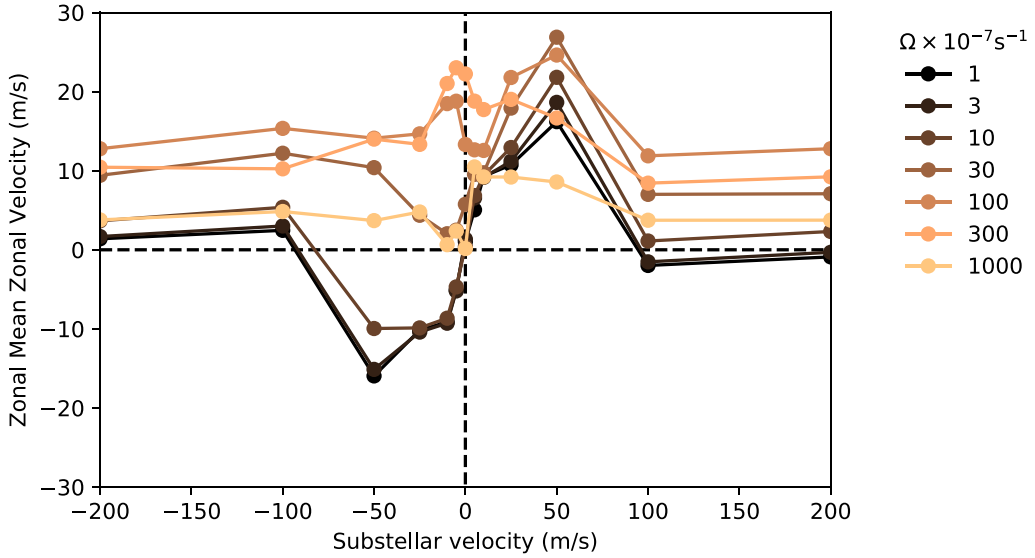

Figure 8. Zonal-mean zonal wind in the upper troposphere ($p = 319$ hPa) as a function of the substellar velocity at the equator. Negative substellar velocity is retrograde, relative to the rotation of the planet. As a point of reference, at equinox, Earth would lie at ∼450 m s^{-1}. Lines show increasing planetary rotation rate. The transverse section view of this data for three substellar velocities is shown in Figure 10.

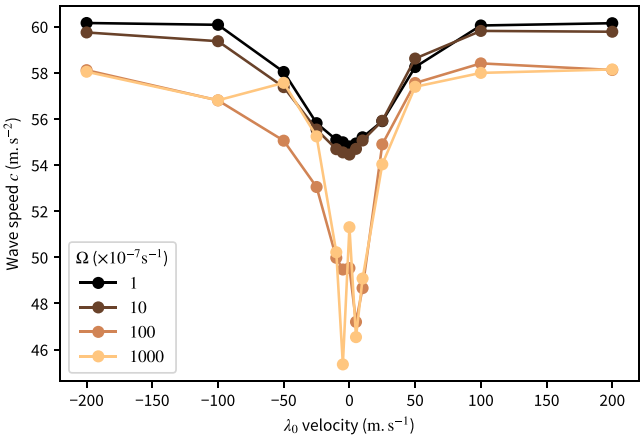

Figure 9. Phase speed of the fastest horizontal mode, $c = NH/\pi$, as a function of substellar velocity (abscissa) and increasing rotation rate (lines).

thermal structure of the atmosphere will largely resemble the forcing, with significant zonal temperature gradients. The redistributive effects of advection and the diurnal cycle act to reduce zonal variation, as seen in the upper rows of Figure 13, where divergent advection from the substellar point efficiently redistributes heat globally.

There is a case study from our own solar system where the radiative and diurnal timescales are potentially of similar order: Venus.

Venus rotates slowly compared to Earth, $\Omega_{\rm Venus} = 3 \times 10^{-7}$ s^{-1}, and the planet spins in the opposite direction to its orbit. The result is a slow diurnal cycle, approximately 116 Earth days for a single solar day on Venus, and the substellar point moves prograde relative to the rotation of the planet. This corresponds to a substellar velocity on the Venusian equator of $s_{\rm Venus} = 3.8$ m s^{-1}, putting it within the region of parameter space in which we have shown that, for an Earth-like planet at least, the diurnal cycle can induce a superrotation.

Atmospheric soundings of the lower atmosphere of Venus show a strong superrotation in the mid-troposphere (Schubert et al. 1980) and an almost isothermal longitudinal distribution of heat, only a few K difference between day and night suggesting a very efficient heat transfer by the winds. Above the cloud deck of Venus, the longwave radiation optical depth is lower, thermal timescales are shorter, and the difference in day- and nightside temperatures is much larger.

The atmospheric column of Venus is very different from that of the Earth-like model used here; the surface pressure of Venus is 92×10^3 hPa, and the atmosphere is so optically thick at this depth that nearly all of the solar heating happens in the atmosphere interior rather than at the surface, as our idealized Newtonian cooling model prescribes here. There are several potential sources of momentum convergence toward Venus's equator capable of inducing superrotation (Read & Lebonnois 2018); while further study in a portion of parameter space more appropriate to Venus is necessary, it seems plausible that the slowly progressing diurnal cycle could enhance the strength of Venus's superrotation.

3.2. Thermal Phase Curves

In our previous study using a shallow-water model of the first baroclinic mode of the atmosphere (Penn & Vallis 2017), we demonstrated that both eastward and westward offsets in the thermal phase curve of a transiting exoplanet could be observed; the offset is sensitive to both absolute planetary rotation rate and the velocity of the substellar point. It was shown that when the normalized substellar velocity $|s/c| < 1$, where $c = \sqrt{gH_e}$ is the linear shallow-water gravity wave speed for a fluid of equivalent depth H_e, a dynamical balance could be maintained between a horizontal thermal gradient and the moving forcing. When a theoretical "thermal phase curve" of the planet was calculated by integrating the height of the shallow-water layer, it exhibited offsets in both zonal directions relative to the substellar point.

In the same manner, we again now calculate phase curves from the stratified model of the atmosphere. Our model, with a

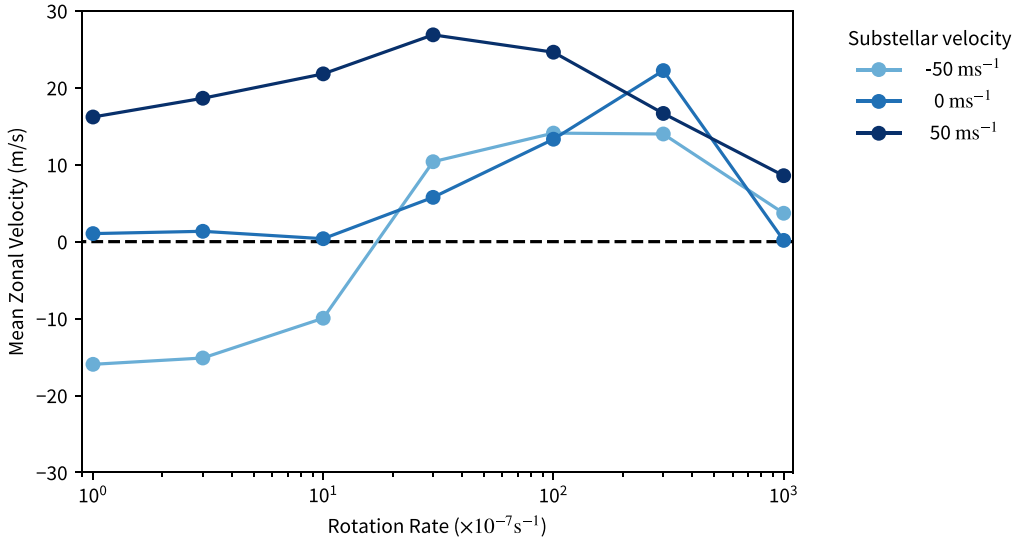

Figure 10. Globally integrated mean zonal wind in the upper troposphere ($p = 319$ hPa) as a function of rotation rate. Lines show the dependence on rotation rate at three substellar velocities: -50, $+50$, and 0 m s^{-1}, corresponding to the local maxima/minima seen in Figure 8.

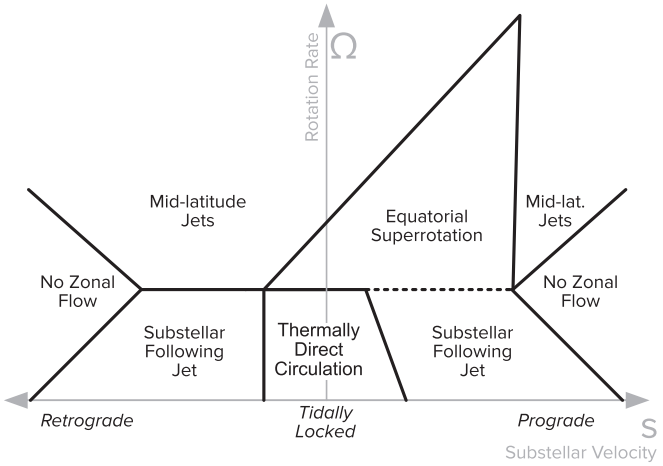

Figure 11. The qualitative regime of the dynamics can be categorized by the nature of the upper-tropospheric flow. This regime diagram classifies the circulation patterns observed across the parameter space of varying planetary rotation rate Ω and substellar velocity s. The dashed line between sections on the right shows that this transition is somewhat continuous, as when the substellar point is moving prograde, a jet in the same direction as the substellar motion, and equatorial superrotation are equivalent.

prescribed relaxation temperature rather than diagnostic radiative heating, does not have an optical depth, nor does it need to satisfy an energy balance by radiating to space. Therefore, there is no well-defined diagnostic OLR, and we use an approximation to this to calculate a thermal phase curve.

We choose a radiating pressure level, $p_{\rm rad}$, as the height of emission to space. At this level, we can create a phase curve by performing a hemispheric integral of blackbody emission,

$$I(\delta; p_{\rm rad}) = \int_{\delta-\pi/2}^{\delta+\pi/2}\int_{-\pi/2}^{\pi/2} a^2\sigma T^4(\lambda, \phi, p_{\rm rad})\cos\lambda\cos^2\phi d\phi d\lambda, \quad (21)$$

where δ is the observational zenith longitude, and σ is the Stephan–Boltzmann constant. The $\cos\lambda\cos\phi$ factor comes from the projection of the curved surface of the planet onto a flat observational disk—the emission received is proportional to the distance from the center of the disk.

The phase curve is normalized by the hemispheric integral of the nightside of the planet equilibrium temperature, $T_{\rm strat}$, and by moving into the reference frame of the moving substellar forcing,

$$\hat{I}(\delta; p_{\rm rad}) = \int_{\delta-\pi/2}^{\delta+\pi/2}\int_{-\pi/2}^{\pi/2}\left(\frac{T(\xi, \phi, p_{\rm rad})}{T_{\rm strat}}\right)^4\cos\xi\cos^2\phi d\phi d\xi, \quad (22)$$

where $\xi = \lambda - \lambda_0(t)$ and the observational zenith longitude, δ, is now relative to the substellar point (see Figure 12 for examples of the temperature field and synthetic thermal phase curve for tidally locked exoplanets with varying rotation rate).

We first consider the thermal response in three dimensions before addressing the contraction of this into a one-dimensional phase curve. Figure 13 presents the atmospheric temperature in the mid-troposphere, just above the prescribed frictional boundary layer, for varying rotation rates and substellar velocities.

In the stratified model, we find a more complicated relationship than in the shallow-water study. At the surface, the thermal response is tightly coupled to the forcing, and at all rotation rates, the peak integrated temperature is lagging the motion of the substellar point. However, at altitude, from where observed infrared emission will originate, the temperature distribution is sensitive to the speed of the diurnal cycle.

Above the boundary layer, momentum and temperature are less strongly damped, thermal advection is efficient compared to friction, and the hot spot is advected by the wind field. Figure 13 shows the horizontal temperature structure in the mid-troposphere; for both eastward- and westward-propagating substellar points, eastward and westward hot spots are observed, depending on the rotation rate of the planet.

As previously demonstrated in the hot Jupiter studies of Showman et al. (2015), a quickly moving substellar point, or rapidly rotating system results in a reduction in zonal variability. At the mid-troposphere example plots shown in Figure 13, there is an $\sim$65 K gradient between substellar and antistellar points in the equilibrium temperature $T_{\rm eq}$; in contrast, the atmospheric temperature varies little, with an efficient

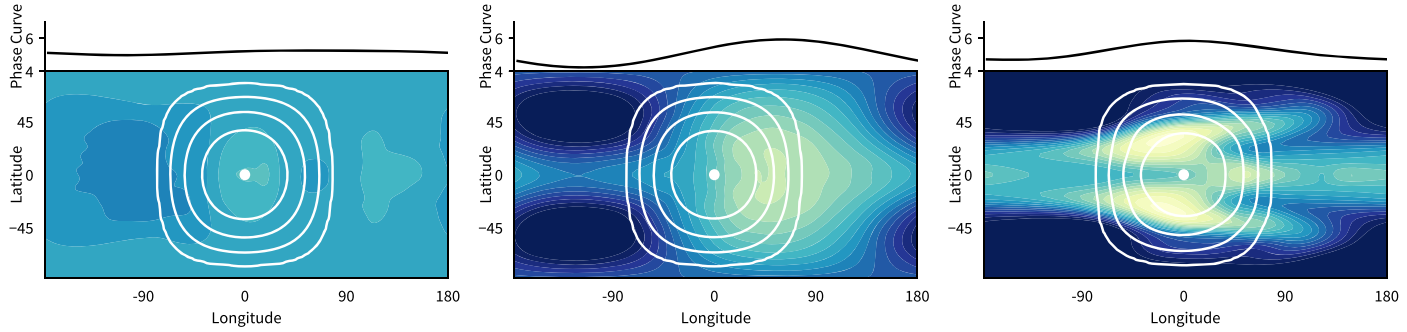

Figure 12. Example temperature fields and their associated normalized phase curves. From left to right, these correspond to $\Omega = 10$, 100, and 1000×10^{-7} s^{-1} in the central, $s = 0$ m s^{-1}, column of Figure 13. The brightest color contour is 260 K, with further contours decreasing in 2 K intervals. White contours show the position and extent of the relaxation temperature profile $T_{\rm eq}$, and the maximum of this at the substellar point is indicated with a white dot. The phase-curve offset is given by the longitudinal separation between the substellar point and the peak of the phase curve, most clearly observed as a westward offset in the middle panel.

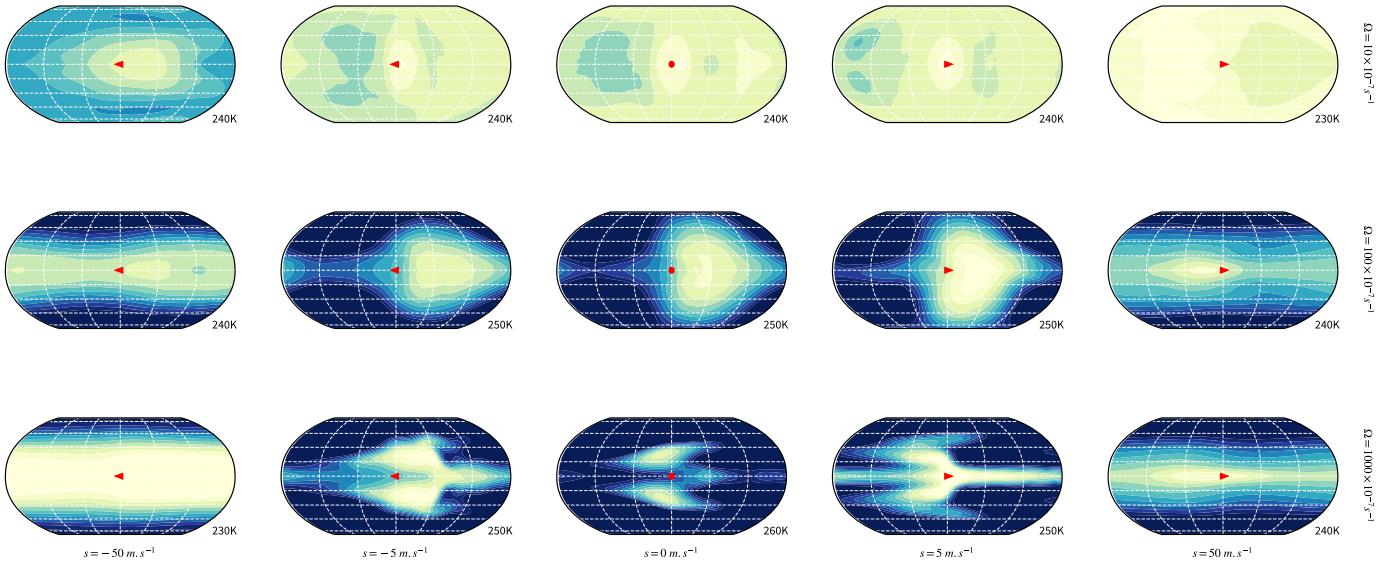

Figure 13. Mid-tropospheric atmospheric temperature ($p = 658$ hPa). The temperature reference in the lower right corner of each pane indicates the value of the highest temperature contour, with successive cooler contours at 2 K intervals. The central column (tidally locked) phase-curve examples are shown in Figure 12. At this height in the atmosphere, $\tau_{\rm rad} = 20$ days, there is no frictional damping.

thermal transport from dayside to nightside. The efficient heat transport and zonal redistribution with a rapidly moving substellar velocity predicts relatively warm nightside temperatures and a largely isothermal distribution of temperature in the upper atmosphere; this is perhaps expected from our intuition of Earth, which has a very rapid diurnal cycle relative to atmospheric radiative timescales, $\tau_{\rm diurnal} \ll \tau_{\rm rad}$. The reduction in the meridional temperature gradient is also a result of the short diurnal timescale, providing an effective relaxation profile, as shown in Figure 7 and discussed above.

The phase-curve offset is found by calculating the normalized phase curve relative to the substellar point using Equation (22) and then solving for the longitude of maximum integrated thermal emission. The panels of Figure 14 show the phase-curve offset as a function of substellar velocity near the surface and at several levels in the troposphere. Phase curves near the surface are a strong function of substellar velocity, with little influence from rotation rate; in general, the faster the substellar point moves, the further the thermal hot spot has lagged behind the point of maximal heating. This is due to the short timescales of both radiative and frictional damping in the bottom boundary of the model; wind velocity at this level is small, resulting in little advection, and strong relaxation toward the heating profile quickly eliminates thermal inertia from the passing substellar point. It was previously shown (Penn & Vallis 2017) that in the simple case of a linear nonrotating one-dimensional shallow-water model heated periodically along the equator, the offset between forcing and response, ξ_p, is given by the form

$$\xi_p = \arctan\left(\frac{(c^2 - s^2)\tau_{\rm rad}}{s}\right), \tag{23}$$

where c is the shallow-water gravity wave speed, which tends to a finite limit of a half-phase lagging offset between forcing and substellar point as the substellar velocity increases in either direction (see Figure 15),

$$\lim_{s \to \mp\infty} \xi_p = \pm\pi/2.$$

However, it also has a maximum as we approach the tidally locked

$$\lim_{s \to \pm 0} \xi_p = \pm\pi/2,$$

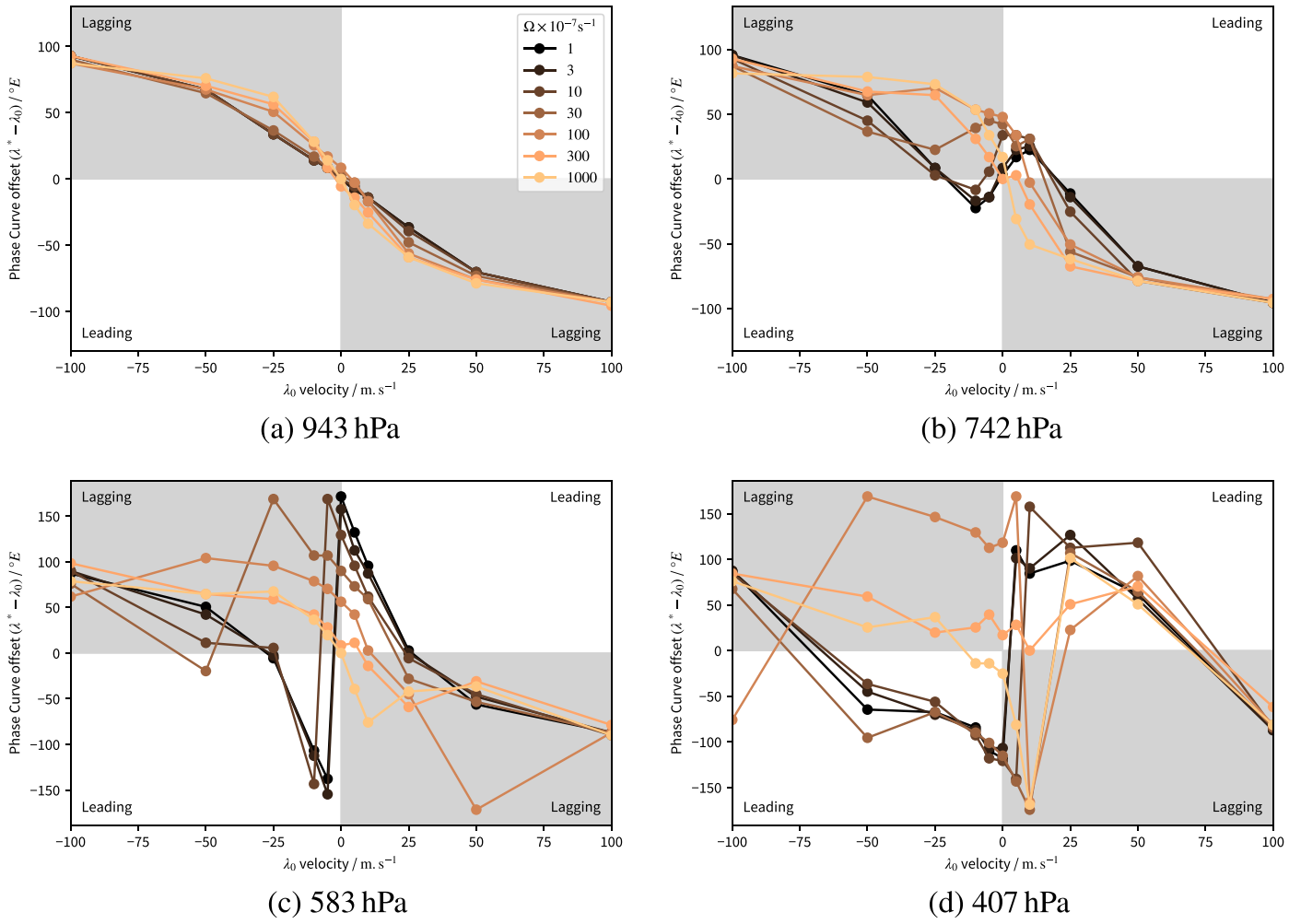

Figure 14. Phase-curve offsets for thermal emission from different heights in the atmosphere as a function of substellar velocity s (abscissa). Lines of increasing brightness show the response at increasing planetary rotation rate. The segments where the thermal hot spot leads the progression of the substellar point (e.g., eastward substellar motion, eastward hot-spot offset) are shaded white, and the lagging segments are shaded gray.

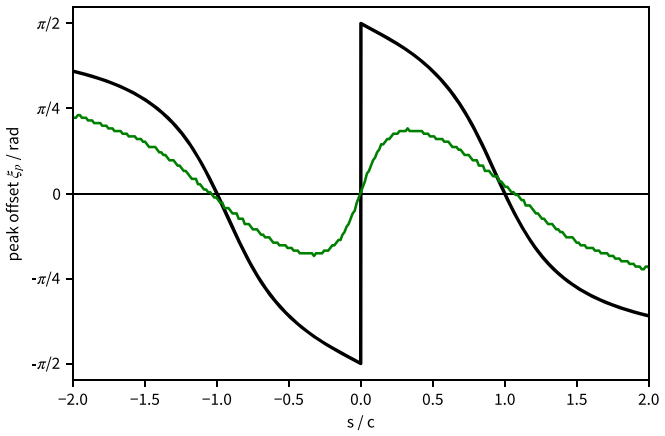

Figure 15. Analytic phase-curve offset for an analogous one-dimensional shallow-water model along the equator in the absence of rotation. The black line is Equation (23), and the green line shows the results of a numerical simulation that includes nonlinear terms, momentum drag, and a nonsmooth forcing similar in form to Equation (12).

a discontinuous leading offset that becomes smooth through the tidally locked state with the addition of nonlinear effects. This character of the response is retained in the stratified model, lagging responses tending to a $\pi/2$ limit in the case of fast substellar motion. In the troposphere, where frictional damping is not applied and the timescale of thermal relaxation is much longer (panels (c) and (d) of Figure 14), a leading offset up to 20° is seen for both prograde and retrograde moving diurnal cycles on slowly rotating planets expected from the shallow-water theory. Where Ro < 1, the circulation becomes increasingly constrained to equatorial regions, equatorially trapped Rossby gyres are seen as temperature maxima above and below the equator, and a trapped Kelvin wave is just east of the substellar point (The effect of these trapped waves most clearly shown in their impact on the integrated thermal phase curve in the last panel of Figure 12).

In the upper atmosphere, all our Newtonian cooling models show a largely isothermal response in all directions, the magnitude of $\Delta T_{\mathrm{day-night}}$ becomes negligible, and the offset becomes highly variable and dominated by synoptic changes.

The model presented here shows that it is possible to observe both an eastward and a westward offset in the observed thermal phase curve of an exoplanet, with few assumptions made about the composition of the atmosphere beyond the heat capacity and gravitational constants of Earth. The simple forcing parameterization offers both advantages and disadvantages in this respect. The relaxation is linear in temperature, scaling the

atmospheric height appropriately, so we might expect the results to hold at hotter temperatures of some of the already observed close-in exoplanets. The assumptions we make about the composition of the atmosphere determine the lapse rate of the equilibrium profile and the internal gravity wave speed; the effect of changing the shape of this vertical profile to that of, e.g., an H/He atmosphere would be an interesting extension.

In the disadvantages column, the lack of a strict energy balance or a two-steam radiation scheme means that the thermal emission of the model can only be considered at a specific height within the atmospheric column. An observed multiband phase curve will be composed of radiation emitted from more than one height in the atmosphere, and this cannot be directly compared to a single height in the atmosphere (Dobbs-Dixon & Cowan 2017); the exact contribution through height is sensitive to temperature, pressure, and chemical composition. As Figure 14 shows, the phase-curve offset observed is dependent on the height within the atmosphere at which it is measured. More complex models have addressed the hot spot of specific exoplanet candidates and found that the offset can vary significantly depending on the radiating level of the atmosphere (Hammond & Pierrehumbert 2017, for example). An interesting further step would be to pass the temperature–pressure profiles of the results shown above to a radiation code to calculate a true thermal emission field. This would require making further choices about the composition of the atmosphere that are beyond the scope of this idealized study.

4. Conclusions

We have used a Newtonian cooling/Rayleigh friction model of the atmosphere to simulate a suite of Earth-like exoplanets in the parameter regime around a state of tidal locking. We showed that the offset in the thermal phase curve is affected by both the rotation rate and diurnal cycle of the planet, with eastward and westward offsets from the substellar point observed at a range of parameter values. Linking this to an observed phase curve is not necessarily straightforward, however; care must be taken when making further inferences, as the offset also has a strong dependence on the depth within the atmosphere from which the thermal emission originated.

Upper-tropospheric zonal winds are sensitive to both the rotation rate and diurnal period of the planet; even a small amount of asynchronous rotation can induce large changes in the circulation, for example, inhibiting the formation of the equatorial superrotating jet predicted by many tidally locked exoplanet models. In the tidally locked state, a robust superrotating equatorial jet is observed over a range of rotation rates typical of a planet in a 5–100 day orbit. However, with only a small deviation from the tidally locked state producing a moving diurnal heating pattern, the superrotating equatorial jet can be split into midlatitudinal jet streams. The effect of the diurnal cycle on atmospheric dynamics is most pronounced when the substellar velocity has a similar magnitude to the internal wave speed of the stratified atmosphere, depositing momentum into jets in the same direction as the moving forcing, either constructively strengthening the superrotation (in the case of an eastward moving forcing) or destructively weakening it (for a westward moving substellar forcing).

This study demonstrated that asynchronous rotation, even when it is close to being synchronous, can be crucial in understanding the large-scale circulation of a planet's atmosphere. As our methods of detection improve and we discover terrestrial planets further from their host star, with exomoons, and/or with thick Venusian atmospheres, the likelihood of asynchronous rotation increases, and with it comes a whole new range of interesting dynamical regimes to be explored.

References

Cooper, C., & Showman, A. 2006, ApJ, 649, 1048
Demory, B.-O., Gillon, M., de Wit, J., et al. 2016, Natur, 532, 207
Dobbs-Dixon, I., & Cowan, N. 2017, ApJL, 851, L26
Edson, A., Lee, S., Bannon, P., Kasting, J., & Pollard, D. 2011, Icar, 212, 1
Gill, A. 1980, QJRMS, 106, 447
Hammond, M., & Pierrehumbert, R. T. 2017, ApJ, 849, 152
Held, I., & Suarez, M. 1994, BAMS, 75, 1825
Heng, K., Menou, K., & Phillipps, P. 2011, MNRAS, 413, 2380
Hide, R. 1969, JAtS, 26, 841
Ingersoll, A., & Dobrovolskis, A. 1978, Natur, 275, 37
Kaspi, Y., & Showman, A. 2015, ApJ, 804, 60
Kataria, T., Showman, A., Lewis, N., et al. 2013, ApJ, 767, 76
Kiladis, G., Wheeler, M., Haertel, P., Straub, K., & Roundy, P. 2009, RvGeo, 47, RG200342
Knutson, H., Charbonneau, D., Allen, L., et al. 2007, Natur, 447, 183
Komacek, T., & Showman, A. 2016, ApJ, 821, 16
Kopparapu, R., Wolf, E., Haqq-Misra, J., et al. 2016, ApJ, 819, 84
Kraucunas, I., & Hartmann, D. 2005, JAtS, 62, 371
Leconte, J., Wu, H., Menou, K., & Murray, N. 2015, Sci, 347, 632
Lindzen, R. 1981, JGR, 86, 9707
Matsuno, T. 1966, J. Meteorol. Soc. Jpn. Ser. II, 44, 25
Menou, K., & Rauscher, E. 2009, ApJ, 700, 887
Merlis, T., & Schneider, T. 2010, JAMES, 2, 13
Mills, S., & Abbot, D. 2013, ApJL, 774, L17
Noda, S., Ishiwatari, M., Nakajima, K., et al. 2017, Icar, 282, 1
Penn, J., & Vallis, G. 2017, ApJ, 842, 101
Rauscher, E., & Kempton, E. 2014, ApJ, 790, 79
Read, P., & Lebonnois, S. 2018, AREPS, 46, 175
Salameh, J., Popp, M., & Marotzke, J. 2018, ClDy, 50, 2395
Schubert, G., Covey, C., Genio, A., et al. 1980, JGR, 85, 8007
Selsis, F., Maurin, A.-S., Hersant, F., et al. 2013, A&A, 555, A51
Showman, A., Fortney, J., Lian, Y., et al. 2009, ApJ, 699, 564
Showman, A., & Guillot, T. 2002, A&A, 385, 166
Showman, A., Lewis, N., & Fortney, J. 2015, ApJ, 801, 95
Showman, A., & Polvani, L. 2011, ApJ, 738, 71
Sobel, A., Nilsson, J., & Polvani, L. 2001, JAtS, 58, 3650
Vallis, G., Colyer, G., Geen, R., et al. 2018, GMD, 11, 843
Vallis, G. K. 2017, Atmospheric and Oceanic Fluid Dynamics (Cambridge: Cambridge Univ. Press)